

# Valley-polarized quantum anomalous Hall effect in van der Waals heterostructures based on monolayer jacutingaite family materials

Xudong Zhu<sup>1,2,\*</sup>, Yuqian Chen<sup>1,2,\*</sup>, Zheng Liu<sup>1,2,†</sup>, Yulei Han<sup>3,‡</sup>, Zhenhua Qiao<sup>1,2,§</sup>

1 ICQD, Hefei National Research Center for Physical Sciences at the Microscale, University of Science and Technology of China, Hefei 230026, China

2 CAS Key Laboratory of Strongly-Coupled Quantum Matter Physics, and Department of Physics, University of Science and Technology of China, Hefei 230026, China

3 Department of Physics, Fuzhou University, Fuzhou 350108, China

Corresponding authors. E-mail: <sup>†</sup>zhengliu@mail.ustc.edu.cn, <sup>‡</sup>han@fzu.edu.cn, <sup>§</sup>qiao@ustc.edu.cn

\*These authors contributed equally to this work.

Received September 25, 2022; accepted November 18, 2022

© Higher Education Press 2023

## ABSTRACT

We numerically study the general valley polarization and anomalous Hall effect in van der Waals (vdW) heterostructures based on monolayer jacutingaite family materials  $\text{Pt}_2\text{AX}_3$  ( $A = \text{Hg, Cd, Zn}$ ;  $X = \text{S, Se, Te}$ ). We perform a systematic study on the atomic, electronic, and topological properties of vdW heterostructures composed of monolayer  $\text{Pt}_2\text{AX}_3$  and two-dimensional ferromagnetic insulators. We show that four kinds of vdW heterostructures exhibit valley-polarized quantum anomalous Hall phase, i.e.,  $\text{Pt}_2\text{HgS}_3/\text{NiBr}_2$ ,  $\text{Pt}_2\text{HgSe}_3/\text{CoBr}_2$ ,  $\text{Pt}_2\text{HgSe}_3/\text{NiBr}_2$ , and  $\text{Pt}_2\text{ZnS}_3/\text{CoBr}_2$ , with a maximum valley splitting of 134.2 meV in  $\text{Pt}_2\text{HgSe}_3/\text{NiBr}_2$  and sizable global band gap of 58.8 meV in  $\text{Pt}_2\text{HgS}_3/\text{NiBr}_2$ . Our findings demonstrate an ideal platform to implement applications on topological valleytronics.

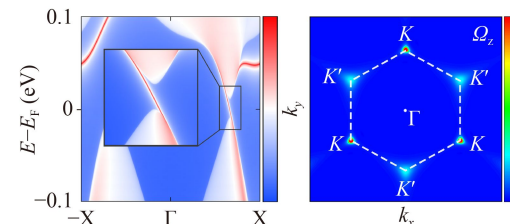
**Keywords** quantum anomalous Hall effect, valley polarization, topological valleytronics, transition metal dichalcogenides, jacutingaite family materials, first-principles calculations, van der Waals heterostructure

## 1 Introduction

The honeycomb lattice materials, such as graphene [1–4] and transition metal dichalcogenides (TMDs) [5–7], host two inequivalent valleys  $K$  and  $K'$  in momentum space located at the corners of the hexagonal Brillouin zone. In addition to the spin of electron, valley is another degree of freedom in two-dimensional honeycomb-like materials. The valley degree of freedom can be tuned by electric fields [8–10], external magnetic fields [11–13], and circularly polarized light excitation [14–16]. Similar to spintronics, valleytronics is mainly focused on manipulating valley

degree of freedom in designing functional nanodevices [17–20], such as electron beam splitter, valley filter, and valley valves [21–25].

Quantum anomalous Hall effect (QAHE) is the quantized version of Hall effect without applying external magnetic fields [26–29], and has been experimentally realized in various material systems [30–33]. The valley polarization, e.g., in TMD materials, is often topologically trivial [34–37], whereas QAHE is usually a valley degenerated state. To implement valley-polarized QAHE, the inversion symmetry and time-reversal symmetry should be simultaneously broken. One rational way to realize



valley-polarized QAHE is by inducing the magnetic proximity effect in the  $\mathbb{Z}_2$  topological insulator/ferromagnetic insulator heterostructures [38–43]. Although several valley-polarized QAHE systems have been theoretically proposed [38–47], more experimentally realizable candidates are still highly desired to observe the valley-polarized QAHE.

In this article, we propose an ideal platform to realize valley polarization and valley-polarized QAHE based on monolayer jacutingaite family materials. Jacutingaite ( $\text{Pt}_2\text{HgSe}_3$ ) is a natural mineral with large intrinsic spin-orbit coupling (SOC). The atomic structure of jacutingaite can be treated as a quarter of  $X$  atoms ( $X = \text{S}, \text{Se}, \text{Te}$ ) of the 1T-phase TMD  $\text{Pt}_X_2$  replaced by  $A$  atoms ( $A = \text{Cd}, \text{Hg}, \text{Zn}$ ), and the monolayer is crystallized in  $P\bar{3}m1$  space group (No. 164) with a buckled honeycomb lattice. The dynamically stable monolayer  $\text{Pt}_2\text{HgSe}_3$  and its family materials  $\text{Pt}_2AX_3$  ( $A = \text{Hg}, \text{Cd}, \text{Zn}; X = \text{S}, \text{Se}, \text{Te}$ ) are  $\mathbb{Z}_2$  topological insulators [48–55]. The monolayer ferromagnetic substrates, i.e.,  $MY_2$  ( $M = \text{Fe}, \text{Co}, \text{Ni}; Y = \text{Cl}, \text{Br}, \text{I}$ ),  $\text{CI}_3$ ,  $\text{VI}_3$ , and  $\text{MnBi}_2\text{Te}_4$ , are used to induce magnetic exchange interactions [56–71]. These two-dimensional magnets possess the ferromagnetic ground states in freestanding monolayer under the Curie temperatures as summarized in Table S2 [72]. By performing first-principles calculations, we systematically investigate the atomic, electronic, and topological properties of over 100 kinds of  $\text{Pt}_2AX_3$ /ferromagnetic substrate van der Waals (vdW) heterostructures. By examining the lattice mismatch, stacking configuration, and band alignment, 44 kinds of well-matched vdW heterostructures are selected. Further analyses on band structures and topological properties demonstrate that these systems host valley polarization and exhibit different Berry curvature distributions at  $K/K'$  valleys.

In particular, we observe valley-polarized QAHE in  $\text{Pt}_2\text{HgS}_3/\text{NiBr}_2$ ,  $\text{Pt}_2\text{HgSe}_3/\text{CoBr}_2$ ,  $\text{Pt}_2\text{HgSe}_3/\text{NiBr}_2$ , and  $\text{Pt}_2\text{ZnS}_3/\text{CoBr}_2$ , with the Chern number of  $C = \pm 1$ . We find a large valley splitting of 134.2 meV in  $\text{Pt}_2\text{HgSe}_3/\text{NiBr}_2$  heterostructure and a considerable topological band gap of 58.8 meV in  $\text{Pt}_2\text{HgS}_3/\text{NiBr}_2$  heterostructure. Both the monolayer jacutingaite family materials and the two-dimensional ferromagnetic substrates are energetically and dynamically stable [53, 56–60], greatly facilitating the experimental implementation of valley-polarized QAHE. Moreover, the structural stabilities of these  $\text{Pt}_2AX_3$ -based vdW ferromagnetic heterostructures are also verified by molecular dynamic simulations [72].

## 2 Calculation methods

Our first-principles calculations were performed by using the projected augmented-wave method [73] as implemented in the Vienna *ab initio* simulation package (VASP) [74, 75]. The generalized gradient approximation of the

Perdew-Burke-Ernzerhof (PBE) type was used to describe the exchange-correlation interaction [76]. The vdW interaction was treated by using DFT-D3 functional [77]. All atoms were fully relaxed until the Hellmann-Feynman force on each atom was less than 0.01 eV/Å. A vacuum buffer layer of 20 Å was used to avoid unnecessary interaction along  $z$  direction between adjacent slabs. The plane-wave energy cutoff was set to be 520 eV. The  $\Gamma$ -centered Monkhorst-Pack  $k$ -point grid of  $11 \times 11 \times 1$  was adopted in all our calculations. To deal with the strong correlation effect of 3d magnetic elements (i.e., Fe, Co, Ni, Cr, V, and Mn), the GGA+ $U$  method [78] was used with the corresponding on-site repulsion energy  $U$  and exchange interaction  $J$  [60–64] as described in Table S1 in supplemental materials [72]. Topological properties were calculated by using maximally-localized Wannier functions as implemented in Wannier90 and WannierTools software packages [79–81]. Spin-resolved band structures are extracted by using VASPKIT software [82] and PYPROCAR code [83]. Atomic structure and charge density difference are visualized by using VESTA software package [84].

## 3 Atomic structures

Monolayer  $\text{Pt}_2AX_3$  ( $A = \text{Hg}, \text{Cd}, \text{Zn}; X = \text{S}, \text{Se}, \text{Te}$ ) is crystallized in  $P\bar{3}m1$  space group (No. 164) with a buckled honeycomb structure as shown in Fig. 1(a). The  $A$  atoms are located at two different sublattices  $A1$  and  $A2$ . The jacutingaite family monolayer  $\text{Pt}_2AX_3$  belongs to Kane-Mele type topological insulator [52, 53], with the maximum band gap of 178 meV for  $\text{Pt}_2\text{ZnSe}_3$  [53]. The typical band structures of monolayer  $\text{Pt}_2AX_3$  are displayed in Figs. 1(b) and (c), where the Dirac points can be observed at  $K$  and  $K'$  valleys in the absence of SOC [see Fig. 1(b)]. When the SOC is considered, as shown in Fig. 1(c), a topological nontrivial band gap opens up around the two valleys. The valley degeneracy of monolayer  $\text{Pt}_2AX_3$  is protected by the time-reversal symmetry and inversion symmetry, leading to  $\Delta_K = \Delta_{K'}$ .

In our calculations, we adopt  $1 \times 1 \text{ Pt}_2AX_3$  and different ferromagnetic substrates with suitable supercell to match the lattice constant. For example, the vdW heterostructure as shown in Fig. 1(a) consists of  $1 \times 1 \text{ Pt}_2AX_3$  and  $2 \times 2 \text{ MY}_2$ . To find the well-matched vdW heterostructures, we carry out the lattice mismatch calculations as plotted in Fig. 2 with orange stars and summarized in Table S3 in supplemental materials [72]. Considering the experimental feasibility, we mainly explore the physical properties of 62 kinds of heterostructures with lattice mismatch less than 5% as highlighted in Table S3 [72]. We then investigate the most stable stacking orders of these vdW heterostructures. For  $\text{Pt}_2AX_3/MY_2$ , we consider four stacking orders according to the atom site directly below  $A1$  atoms: (i)

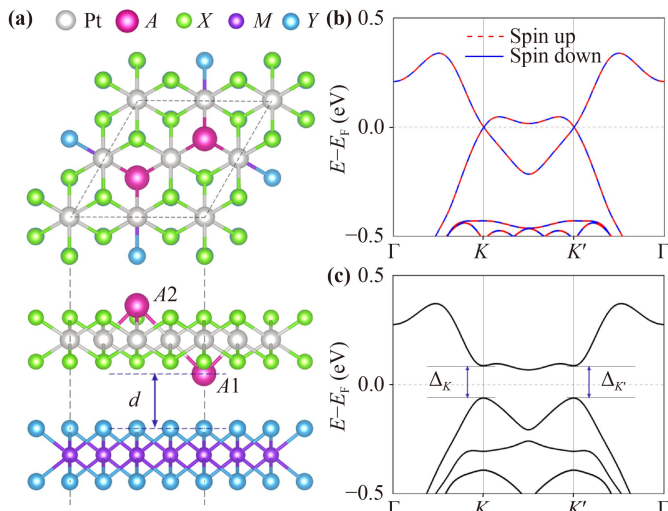


**Fig. 1** (a) Top and side views of  $\text{Pt}_2\text{AX}_3/\text{MY}_2$  heterostructure where  $2 \times 2 \text{ MY}_2$  is adopted to match  $1 \times 1 \text{ Pt}_2\text{AX}_3$ .  $d$  denotes the optimized vdW gap between the ferromagnetic substrate and jacutingaite family monolayer.  $A_1$  and  $A_2$  represent different sublattices of  $A$  atoms, where  $A_1$  locates closer to the ferromagnetic substrate. (b, c) Band structures for the pristine jacutingaite  $\text{Pt}_2\text{HgSe}_3$  monolayer (b) without and (c) with SOC.  $\Delta_K$  and  $\Delta_{K'}$  are local band gaps at valley  $K$  and  $K'$  valleys, respectively.

$M$ , (ii)  $Y$ (top), (iii)  $Y$ (hollow), and (iv)  $MY$ (bridge), respectively. Figure 1(a) displays the type-i stacking configuration and the other three configurations are displayed in Fig. S3 in supplemental materials [72]. After geometrical optimization and total energy computation for different stacking orders, we summarize the most stable stacking configurations for every well-matched vdW heterostructure in Table S5 in supplemental materials [72].

## 4 Band alignments

To design functional devices based on heterostructures, band alignment is a crucial strategy that is widely used to analyze band edges of the two different materials forming a heterostructure [85, 86]. According to the different band gap positions, band alignment can be specified into three types: (I) straddling gap, (II) staggered gap, and (III) broken gap. Due to the type-III band alignment leading to the absence of global band gap in a heterostructure [87, 88], we apply the band alignment strategy to screen out the type-I and type-II vdW heterostructures in order to obtain a global band gap.

Figure 2 displays the band alignments of jacutingaite family monolayer  $\text{Pt}_2\text{AX}_3$  with different ferromagnetic substrates, which are obtained by calculating the work function and band structures of each freestanding material. We first take  $\text{Pt}_2\text{HgS}_3$  as an example to analyze the band alignment. The first column in Fig. 2(a) represents

the band edge of monolayer  $\text{Pt}_2\text{HgS}_3$ , and the Fermi level (dashed red line) with respect to the vacuum level (0 eV) is about  $-5$  eV lying inside the intrinsic band gap as displayed in gray region. The blue (white) area represents the presence (absence) of electronic states. One can find that the band gap of  $\text{Pt}_2\text{HgS}_3$  layer lies in the band gap of  $\text{NiBr}_2$ , resulting in a type-I heterostructure of  $\text{Pt}_2\text{HgS}_3/\text{NiBr}_2$ . Similarly, the  $\text{Pt}_2\text{HgS}_3/\text{FeBr}_2$  system follows the type-II band alignment with the staggered gap. However, the  $\text{Pt}_2\text{HgS}_3/\text{NiCl}_2$  system demonstrates the type-III nature because of the broken gap alignment, which will be excluded in our following discussions. By combining the band alignment and lattice mismatch analyses, we can filter out 44 kinds of vdW heterostructures from over 100 combinations as summarized in Table S5 in supplemental materials [72], in which we hopefully obtain global band gaps with Chern insulating phase after these heterostructures are formed.

## 5 Interfacial electronic and magnetic properties

When two different materials form heterostructures, the charge transfer process usually exists and further modifies the electronic and magnetic properties of the heterostructure [89–91]. To explore the interfacial electronic properties of the  $\text{Pt}_2\text{AX}_3$ /ferromagnetic insulator vdW heterostructures, we calculate the charge density difference and the planar-averaged electrostatic potential along  $z$  direction. Here, we take eight typical systems with  $\text{CoBr}_2$  and  $\text{NiBr}_2$  substrates to illustrate the charge transfer process as shown in Fig. 3, Table 1 and Figs. S10 and S11 in supplemental materials [72].

For  $\text{Pt}_2\text{HgSe}_3/\text{NiBr}_2$ , as displayed in Fig. 3(a), the planar-averaged electrostatic potential along  $z$  direction in  $\text{Pt}_2\text{HgSe}_3$  layer is no longer symmetric with respect to the  $\text{Pt}$  atomic layer, indicating the presence of charge transfer process at the interface. More quantitatively, the Bader charge analysis demonstrates the transferred charge  $\Delta Q$  from  $\text{NiBr}_2$  layer to  $\text{Pt}_2\text{HgSe}_3$  layer is  $-0.11e$ . The charge density difference, as illustrated in Fig. 3(b), also demonstrates that the  $\text{NiBr}_2$  layer accumulates electrons whereas the  $\text{Pt}_2\text{HgSe}_3$  layer loses electrons after they form a heterostructure. As a result, a built-in electric field  $\Delta V_z$  appears at the interface as displayed in Fig. 3(a), which can further enhance the Rashba SOC of the  $\text{Pt}_2\text{HgSe}_3/\text{NiBr}_2$  system.

Table 1 displays the transferred charge  $\Delta Q$ , vdW gap  $d$ , and magnetic moments of the eight typical  $\text{Pt}_2\text{AX}_3/\text{MY}_2$  vdW heterostructures. One can observe that all the interlayer vdW gaps  $d$  become smaller than the initial state after full structural relaxation. Due to the smaller atomic radius of  $S$  atom compared to  $\text{Se}$  atom,  $\text{Pt}_2\text{HgS}_3$  tends to move closer to the substrate than  $\text{Pt}_2\text{HgSe}_3$  when constructing a heterostructure with the same

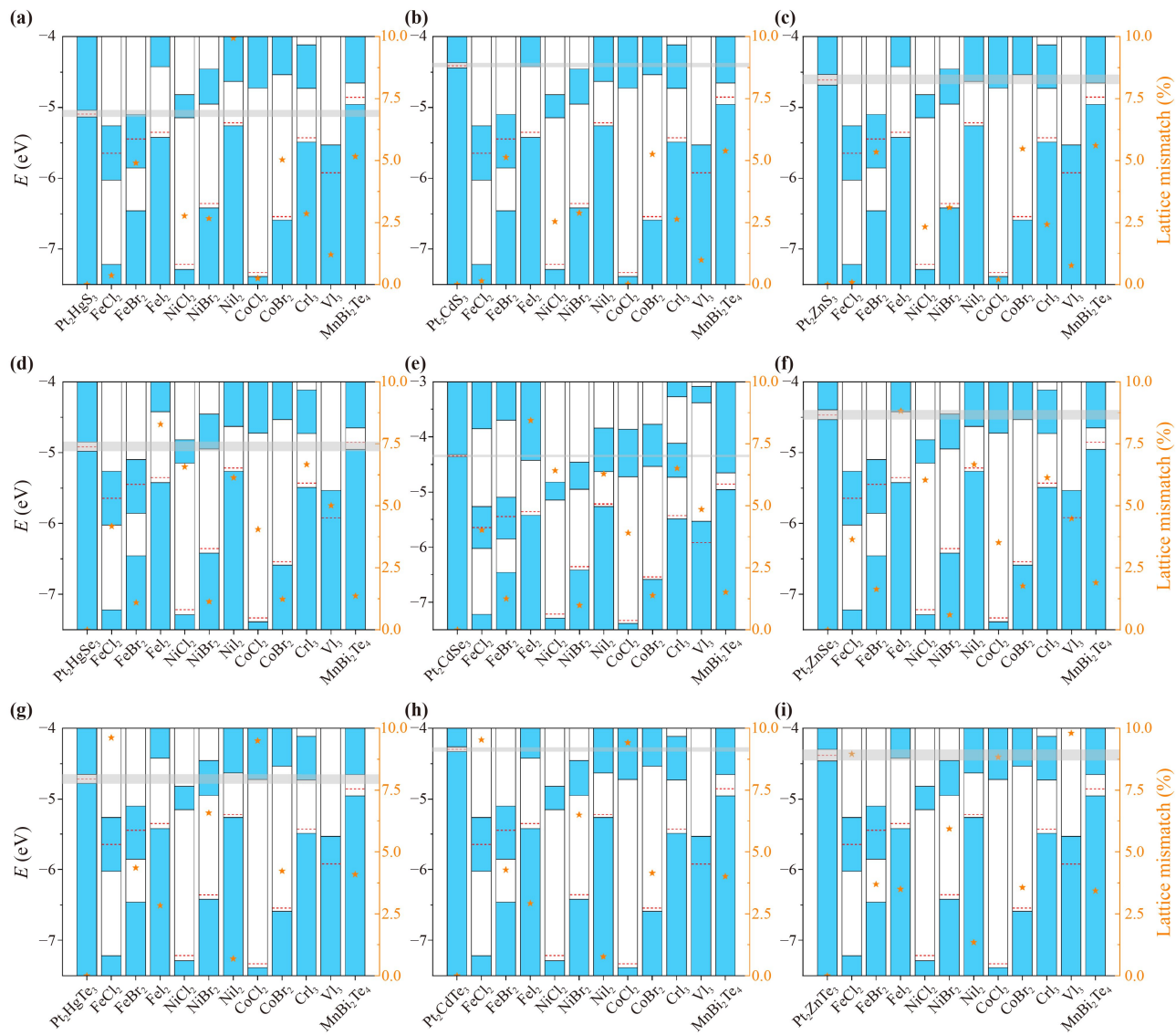


**Fig. 2** Band alignments and lattice mismatch of jacutingaite family monolayer  $\text{Pt}_2\text{AX}_3$ /ferromagnetic substrate heterostructures. Gray region stands for the intrinsic band gap of each jacutingaite family monolayer  $\text{Pt}_2\text{AX}_3$ . The blue (white) area represents the presence (absence) of electronic states. Band edges are relative to the vacuum level by calculating work functions (dashed red line). Orange star (right axis) denotes the lattice mismatch of corresponding vdW heterostructure. (a–c), (d–f), and (g–i) represent the cases with  $X = \text{S}, \text{Se}, \text{Te}$ , respectively. (a, d, g), (b, e, h), and (c, f, i) represent the cases with  $A = \text{Hg}, \text{Cd}, \text{Zn}$ , respectively.

**Table 1** Transferred charge  $\Delta Q$ , vdW gap  $d$ , and magnetic moments of 8 kinds of typical  $\text{Pt}_2\text{AX}_3/\text{MY}_2$  vdW heterostructures.  $\Delta Q$  is extracted from the Bader charge analysis to evaluate the transferred electrons from the ferromagnetic substrate to  $\text{Pt}_2\text{AX}_3$  layer.  $d$  represents the interlayer distance after full relaxation.  $M_{\text{jac}}$ ,  $M_{\text{tot}}$ ,  $M_{A1}$ , and  $M_{A2}$  denote the magnetic moment of  $\text{Pt}_2\text{AX}_3$  layer, total vdW heterostructure,  $A1$  atom, and  $A2$  atom, respectively.

vdW Heterostructures	$\text{Pt}_2\text{HgS}_3/\text{CoBr}_2$	$\text{Pt}_2\text{HgSe}_3/\text{CoBr}_2$	$\text{Pt}_2\text{HgTe}_3/\text{CoBr}_2$	$\text{Pt}_2\text{ZnS}_3/\text{CoBr}_2$	$\text{Pt}_2\text{HgS}_3/\text{NiBr}_2$	$\text{Pt}_2\text{HgSe}_3/\text{NiBr}_2$	$\text{Pt}_2\text{CdS}_3/\text{NiBr}_2$	$\text{Pt}_2\text{ZnSe}_3/\text{NiBr}_2$
$\Delta Q$ ( $e$ )	-0.17	-0.20	-0.09	-0.32	-0.03	-0.11	-0.18	-0.17
$d$ ( $\text{\AA}$ )	2.51	2.74	2.90	2.70	2.28	2.46	2.18	2.51
$M_{\text{jac}}$ ( $\mu_B$ )	0.330	0.061	0.068	0.050	0.219	0.204	0.276	0.167
$M_{\text{tot}}$ ( $\mu_B$ )	11.525	11.530	11.490	11.503	7.453	7.446	7.392	7.420
$M_{A1}$ ( $\mu_B$ )	0.005	-0.009	-0.005	-0.014	-0.016	-0.021	-0.020	0.009
$M_{A2}$ ( $\mu_B$ )	0.056	0.016	0.007	0.024	0.067	0.045	0.104	0.027

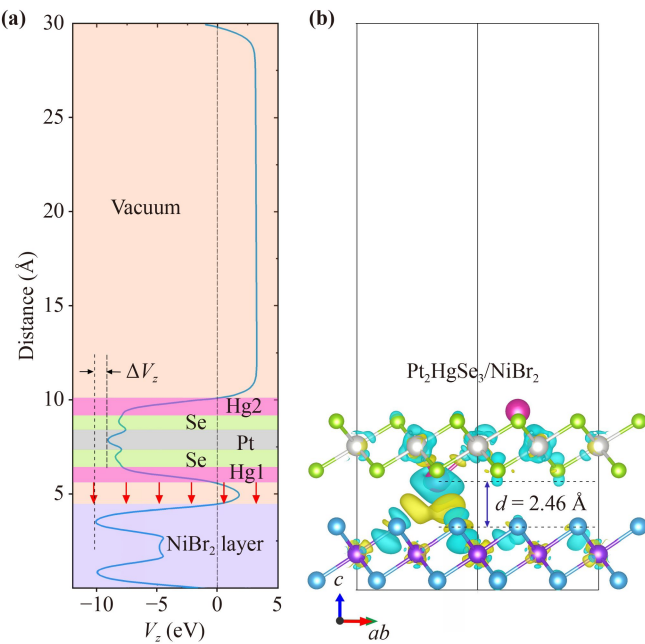


**Fig. 3** (a) The planar-averaged electrostatic potential  $V_z$  and (b) charge density difference of the  $Pt_2HgSe_3/NiBr_2$  heterostructure.  $V_z$  in  $Pt_2HgSe_3$  layer is asymmetric with respect to the  $Pt$  atomic layer, indicating the charge transfer at the interface. Highlighted regions in (a) correspond to associated horizontal atomic layers in (b). Cyan and yellow contours represent charge depletion and accumulation, respectively.

substrate. Moreover,  $d$  in  $Pt_2AX_3/NiBr_2$  is generally smaller than that in  $Pt_2AX_3/CoBr_2$ . The shorter  $d$  in  $Pt_2AX_3/NiBr_2$  leads to a stronger magnetic proximity effect and large magnetization  $M_{\text{Jac}}$  in jacutingaite layer. The magnetic proximity effect also induces different magnetic moments  $M_{A1}$  and  $M_{A2}$  on  $A1$  and  $A2$  because of the different distances to the substrate. The presence of a ferromagnetic substrate breaks both inversion and time-reversal symmetries and leads to inequivalent exchange fields on  $A1$  and  $A2$  atoms, which lifts the spin degeneracy and valley-dependent band gaps. Nonzero Berry curvature and anomalous Hall responses can also appear [38]. For example, in  $Pt_2HgSe_3/NiBr_2$ , the magnetic moment of  $Hg2$  atom is  $0.045 \mu_B$  and is parallel to that of  $NiBr_2$ , whereas an antiparallel magnetic moment of  $-0.021 \mu_B$  is induced in  $Hg1$  atom. Consequently, the valley degeneracy of  $Pt_2AX_3$  can be lifted by the proximity effect induced broken time-reversal symmetry and Rashba SOC. Hereinbelow, we explore the electronic properties of these  $Pt_2AX_3$ /ferromagnetic substrate vdW heterostructures.

## 6 Electronic and topological properties

After calculating band structures and topological properties of the 44 kinds of well-matched  $Pt_2AX_3$ /ferromagnetic

substrate vdW heterostructures, we find four systems are topologically nontrivial, whereas the remaining systems are topologically trivial (see Figs. S12–S22 in supplemental materials [72] for band structures of all 44 systems). Figure 4 shows the spin-resolved and layer-resolved band structures of the four topologically nontrivial systems, i.e.,  $Pt_2HgSe_3/NiBr_2$ ,  $Pt_2ZnS_3/CoBr_2$ ,  $Pt_2HgS_3/NiBr_2$ , and  $Pt_2HgSe_3/CoBr_2$ .

We start from  $Pt_2HgSe_3/NiBr_2$  as an example [see Figs. 4(a)–(c)]. In the absence of SOC, as shown in Fig. 4(a), we can observe that the magnetic proximity effect of ferromagnetic substrates induces sizable Zeeman splitting but keeps the valley degeneracy. Further calculations on the band structures with and without magnetization also demonstrate that the band structures of the  $Pt_2AX_3$  near the Fermi level are modified by the magnetic exchange interaction [72]. When SOC is considered, as displayed in Fig. 4(b), a band inversion appears around  $K'$  point with a band gap of 6.3 meV induced by Rashba SOC, whereas the bands close to the Fermi level around  $K$  point move far away from each other in a repulsive manner, forming a sizable local band gap of  $\Delta_K$  of 182.8 meV. The difference around  $K/K'$  valleys results in a large valley splitting of 134.2 meV. We can also observe from the layer-resolved band structures as shown in Fig. 4(c) that the electronic states near the Fermi level are mainly dominated by the topological  $Pt_2HgSe_3$  layer, indicating the electronic structures of the  $Pt_2HgSe_3$  monolayer are modified after coupled to the  $NiBr_2$  substrate.

The above band analysis can be applied to the remaining three nontrivial systems. For  $Pt_2ZnS_3/CoBr_2$  system, as shown in Figs. 4(d)–(f), the band structures are similar to that of  $Pt_2HgSe_3/NiBr_2$  with a band inversion and a global band gap of 7.8 meV around  $K'$  point induced by Rashba SOC. For  $Pt_2HgS_3/NiBr_2$  and  $Pt_2HgSe_3/CoBr_2$  systems, as illustrated in Figs. 4(g)–(l), the bands are different from that of  $Pt_2HgSe_3/NiBr_2$ , where the local gap at  $K$  valley is smaller than that at  $K'$  valley. Table 2 summarizes the extracted valley splitting  $\Delta$ , global band gaps  $E_g$ , local band gaps  $\Delta_K/\Delta_{K'}$  at valleys  $K/K'$ , and Chern numbers  $C$  for above four vdW heterostructures. One can see that the valley polarization generally exists in these systems (also see Table S5 in supplemental materials [72] for the remaining 40 kinds of heterostructures). Among the 44 systems, the  $Pt_2HgSe_3/NiBr_2$  exhibits the maximum valley splitting of 134.2 meV, which is an order of magnitude larger than experimental observations in TMD/ferromagnetic substrate systems [92, 93], providing an ideal platform to realize topological valleytronics.

To evaluate the topology of the above band structures, we compute the Berry curvature of all occupied bands in each system by using maximally localized Wannier functions [79, 80]. We carry out orbital projections for every insulating system to guide the Wannier functions. For

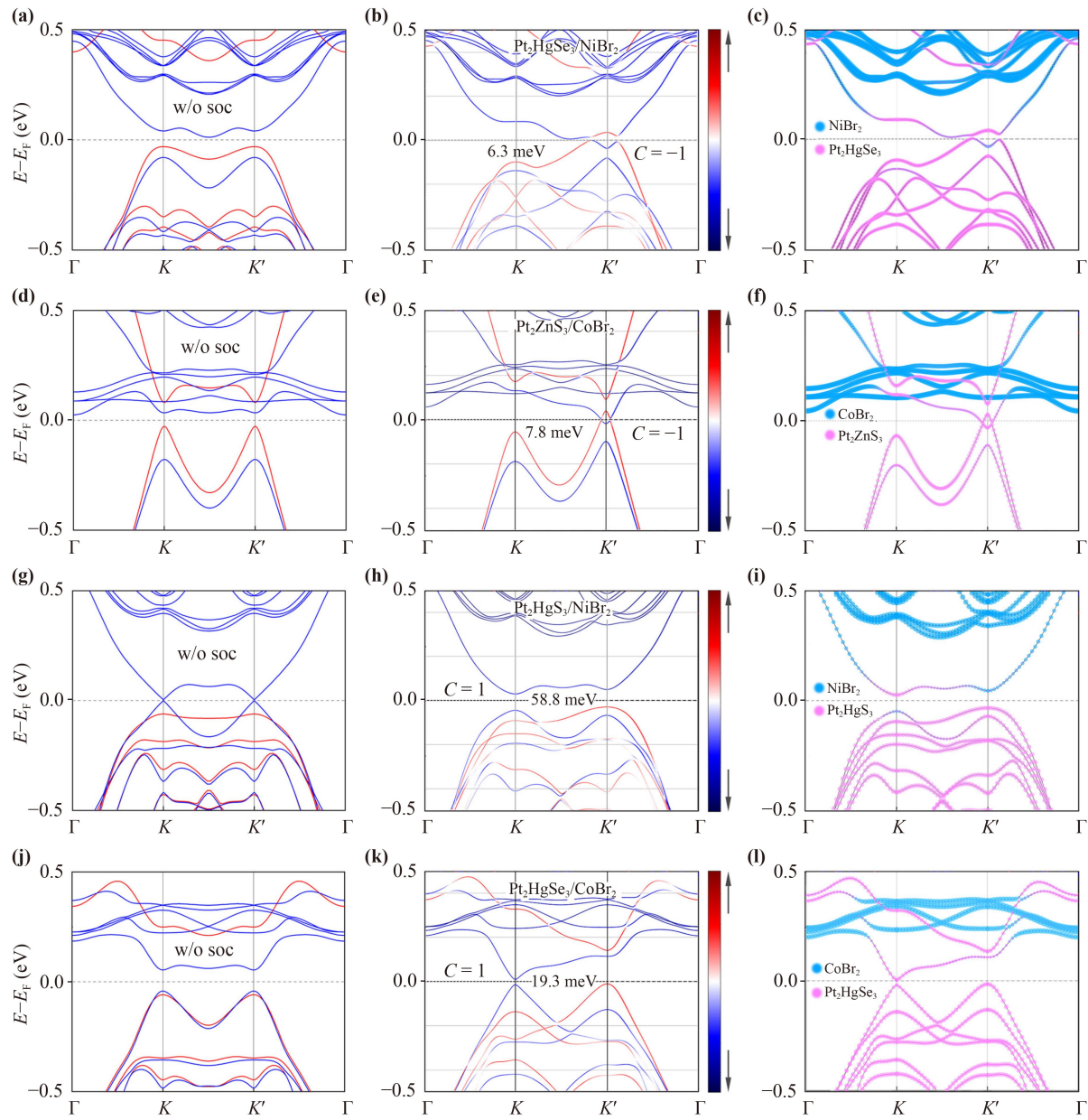


**Fig. 4** (a, b) Spin-resolved band structures of the Pt<sub>2</sub>HgSe<sub>3</sub>/NiBr<sub>2</sub> heterostructure (a) without and (b) with SOC, respectively. (d, e) Spin-resolved band structures of the Pt<sub>2</sub>ZnS<sub>3</sub>/CoBr<sub>2</sub> heterostructure (d) without and (e) with SOC, respectively. (g, h) Spin-resolved band structures of the Pt<sub>2</sub>HgS<sub>3</sub>/NiBr<sub>2</sub> heterostructure (g) without and (h) with SOC, respectively. (j, k) Spin-resolved band structures of the Pt<sub>2</sub>HgSe<sub>3</sub>/CoBr<sub>2</sub> heterostructure (j) without and (k) with SOC, respectively. The red (blue) color denotes the spin-up (spin-down) state. The Chern number  $C$  and the global band gap for every system is demonstrated in (b), (e), (h), and (k), respectively. (c, f, i, l) Layer-resolved band structures of (c) Pt<sub>2</sub>HgSe<sub>3</sub>/NiBr<sub>2</sub>, (f) Pt<sub>2</sub>ZnS<sub>3</sub>/CoBr<sub>2</sub>, (i) Pt<sub>2</sub>HgS<sub>3</sub>/NiBr<sub>2</sub>, and (l) Pt<sub>2</sub>HgSe<sub>3</sub>/CoBr<sub>2</sub>. The pink bubble represents the element projection of jacutingaite family layer whereas the light blue bubble represents the element projection of ferromagnetic substrate layer.

**Table 2** Valley splitting  $\Delta$ , global band gap  $E_g$ , local band gaps  $\Delta_K/\Delta_{K'}$  at  $K/K'$  valleys, and Chern number  $C$  for nontrivial jacutingaite family monolayer/ferromagnetic substrate vdW heterostructures. Valley splitting is evaluated via the difference between valence band maximum at valley  $K/K'$ , i.e.,  $\Delta = E_V(K') - E_V(K)$ .

Nontrivial vdW heterostructures	$\Delta$ (meV)	$E_g$ (meV)	$\Delta_K$ (meV)	$\Delta_{K'}$ (meV)	$C$
Pt <sub>2</sub> HgSe <sub>3</sub> /NiBr <sub>2</sub>	134.2	6.3	182.8	73.5	-1
Pt <sub>2</sub> ZnS <sub>3</sub> /CoBr <sub>2</sub>	36.3	7.8	185.9	59.9	-1
Pt <sub>2</sub> HgS <sub>3</sub> /NiBr <sub>2</sub>	15.4	58.8	74.2	78.8	1
Pt <sub>2</sub> HgSe <sub>3</sub> /CoBr <sub>2</sub>	3.5	19.3	22.8	124.0	1

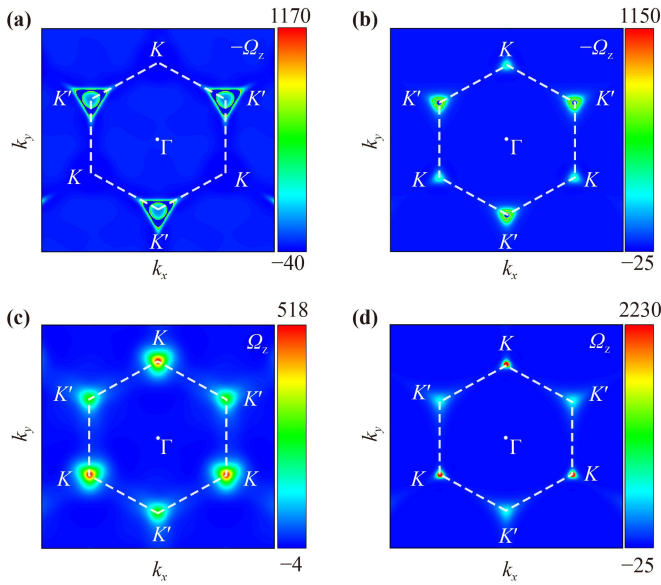


**Fig. 5** Berry curvature distributions in the first Brillouin zone of four nontrivial vdW heterostructures **(a)**  $\text{Pt}_2\text{HgSe}_3/\text{NiBr}_2$ , **(b)**  $\text{Pt}_2\text{ZnS}_3/\text{CoBr}_2$ , **(c)**  $\text{Pt}_2\text{HgS}_3/\text{NiBr}_2$ , and **(d)**  $\text{Pt}_2\text{HgSe}_3/\text{CoBr}_2$ , respectively. Berry curvature is centered around the  $K/K'$  valleys and is absent elsewhere but dissimilarly distributes in the two inequivalent valleys  $K/K'$ . For clarity, (a) and (b) plot  $-\Omega_z$  whereas (c) and (d) plot  $\Omega_z$ .

example, by analyzing the orbital projection on each kind of elements  $\text{Pt}_2\text{HgSe}_3/\text{NiBr}_2$ , we find that Pt-*d*, Hg-*s*, Se-*p*, Ni-*d*, and Br-*p* orbitals are distributed around Fermi level (see Figs. S1–S2 in supplemental materials

[72]). Figure 5 displays the Berry curvature distributions of above four systems in the first Brillouin zone. One can see that the Berry curvature is centered around the  $K/K'$  valleys but is absent elsewhere. The value of the Berry curvature around  $K/K'$  valleys depends on the specific material combinations, i.e., the Berry curvature only appears in  $K'$  valley for  $\text{Pt}_2\text{HgSe}_3/\text{NiBr}_2$  as displayed in Fig. 5(a), while it exists in both  $K$  and  $K'$  valleys with different magnitudes for other three systems as shown in Figs. 5(b)–(d). By integrating the Berry curvature all over the first Brillouin zone, we can obtain the Chern numbers as listed in Table 2. The nonzero Chern number indicates the nontrivial band topology in the four systems, i.e., the formation of QAHE. Combining the valley polarizations and different Berry curvature distributions at the two inequivalent valleys, we can find that these four systems can implement valley-polarized QAHE. More strikingly, the global band gap of 58.8 meV in  $\text{Pt}_2\text{HgS}_3/\text{NiBr}_2$  is over three times larger than that in  $\text{Pt}_2\text{HgSe}_3/\text{CrI}_3$  heterostructure (17.2 meV) as predicted in our previous report [38], implying the potential for high-temperature QAHE [94–99]. Surprisingly, the magnetocrystalline anisotropy energy (MAE) calculation shows that the MAE of  $\text{Pt}_2\text{ZnS}_3/\text{CoBr}_2$  heterostructure is 1.795 meV/Co, suggesting the magnetic easy axis of  $\text{CoBr}_2$  can be tuned by  $\text{Pt}_2\text{ZnS}_3$  to out-of-plane direction [72], which is beneficial to the experimental realization of valley-polarized QAHE.

The nontrivial topology of the four systems can also be confirmed by the anomalous Hall conductance  $\sigma_{xy}$  and the local density of states (LDOS) calculations, as

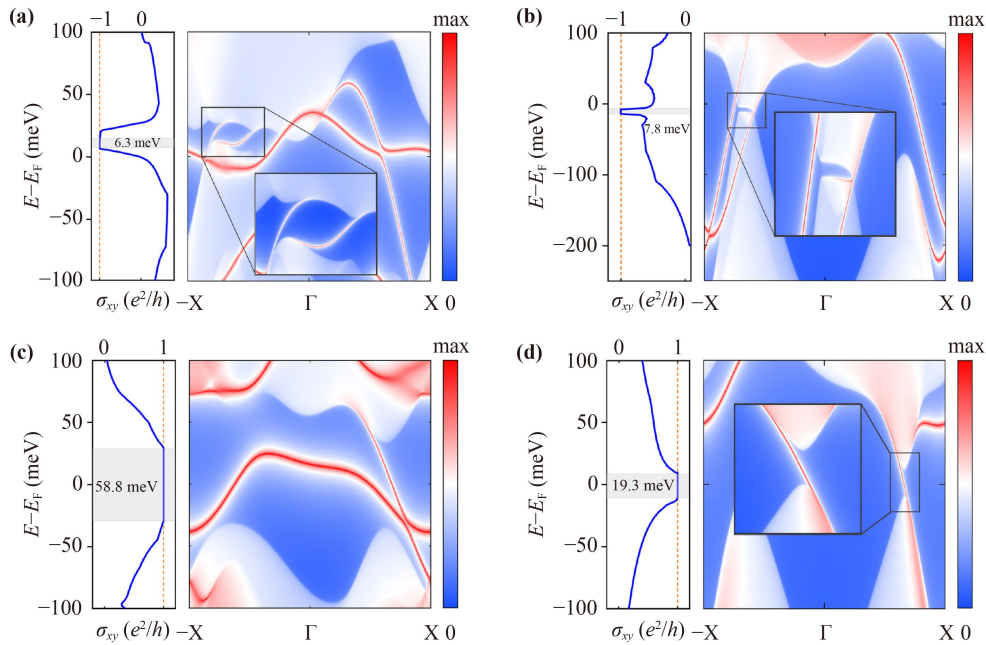


**Fig. 6** Anomalous Hall conductance  $\sigma_{xy}$  and local density of states (LDOS) of four nontrivial vdW heterostructures **(a)**  $\text{Pt}_2\text{HgSe}_3/\text{NiBr}_2$ , **(b)**  $\text{Pt}_2\text{ZnS}_3/\text{CoBr}_2$ , **(c)**  $\text{Pt}_2\text{HgS}_3/\text{NiBr}_2$ , and **(d)**  $\text{Pt}_2\text{HgSe}_3/\text{CoBr}_2$ . Insets correspond to enlarged views of edge states. In all LDOS plots, there are chiral edge states connecting conduction bands and valence bands.

displayed in Fig. 6. The anomalous Hall conductance in Figs. 6(a) and (b) demonstrates a quantized Hall plateau of  $\sigma_{xy} = -e^2/h$  in  $\text{Pt}_2\text{HgSe}_3/\text{NiBr}_2$  and  $\text{Pt}_2\text{ZnS}_3/\text{CoBr}_2$  systems when the Fermi energy lies inside the global band gap, which is a strong evidence for QAHE. Similarly, in Figs. 6(c) and (d), we can also observe that the anomalous Hall conductance is quantized as  $\sigma_{xy} = e^2/h$  in  $\text{Pt}_2\text{HgS}_3/\text{NiBr}_2$  and  $\text{Pt}_2\text{HgSe}_3/\text{CoBr}_2$  systems. Such a Chern insulating topological phase is also confirmed by the LDOS of these nontrivial systems since there are chiral edge states in the global band gaps connecting conduction bands and valence bands.

## 7 Summary and conclusion

In this work, we proposed an excellent platform to implement valley polarization and valley-polarized QAHE based on the vdW heterostructure constructed by monolayer jacutingaite family materials  $\text{Pt}_2AX_3$  and two-dimensional ferromagnetic substrates. We systematically investigated atomic structures, band alignments, interfacial characteristics, electronic and topological properties of over 100 kinds of  $\text{Pt}_2AX_3$ /ferromagnetic substrate heterostructures. By using the band alignment strategy, we filtered out 44 kinds of well-matched systems with potential for global band gaps. We evaluated the interfacial characteristics by analyzing the charge density difference, Bader charge transferring, planar-averaged electrostatic potential, and magnetic properties. The interlayer charge transfer leads to a built-in electric field and the asymmetric atomic structure results in a broken inversion symmetry. Furthermore, the reducing interlayer vdW gap leads to a strong magnetic proximity, which induces large magnetization in Kane–Mele type topological insulator  $\text{Pt}_2AX_3$ . Consequently, the valley degeneracy is lifted by the breaking of time-reversal symmetry and inversion symmetry. We found the general valley polarization in the 44 kinds of well-matched systems and observed a sizable valley splitting of 134.2 meV in  $\text{Pt}_2\text{HgSe}_3/\text{NiBr}_2$  system.

Particularly, we identified four Chern insulators in  $\text{Pt}_2\text{HgS}_3/\text{NiBr}_2$ ,  $\text{Pt}_2\text{HgSe}_3/\text{CoBr}_2$ ,  $\text{Pt}_2\text{HgSe}_3/\text{NiBr}_2$ , and  $\text{Pt}_2\text{ZnS}_3/\text{CoBr}_2$  due to their nontrivial band topology. In addition to the valley polarization, we also observed different Berry curvature distributions in the two inequivalent valleys  $K/K'$  in these four systems, indicating the presence of valley-polarized QAHE. Eventually, we obtained valley-polarized QAHE with total Chern numbers  $C = \pm 1$  in the vdW heterostructures based on monolayer jacutingaite family materials. Most surprisingly, we observed a sizable nontrivial global band gap of 58.8 meV in the  $\text{Pt}_2\text{HgS}_3/\text{NiBr}_2$  system with potential implementation for the high-temperature QAHE.

In conclusion, valley polarization universally exists in the ferromagnetic vdW heterostructures based on mono-

layer jacutingaite family materials and several valley-polarized QAHE vdW heterostructures can be achieved when the valley splitting is strong enough to lead to a band inversion. Our work proposes an excellent platform based on monolayer jacutingaite family materials  $\text{Pt}_2AX_3$  to implement topological valleytronics and may stimulate more applications on the two-dimensional valley-polarized topological systems.

**Electronic supplementary material** Supplementary materials are available in the online version of this article at <https://doi.org/10.1007/s11467-022-1228-4> and <https://journal.hep.com.cn/fop/EN/10.1007/s11467-022-1228-4> and are accessible for authorized users.

**Acknowledgements** We are grateful to Prof. Yang Gao for helpful advice and discussions. This work was financially supported by the National Natural Science Foundation of China (Grant Nos. 11974327 and 12004369), the Fundamental Research Funds for the Central Universities (Nos. WK3510000010 and WK2030020032), and Anhui Initiative in Quantum Information Technologies (Grant No. AHY170000). We also thank for the high-performance supercomputing services provided by AM-HPC and the Supercomputing Center of University of Science and Technology of China.

## References

1. A. K. Geim and K. S. Novoselov, The rise of graphene, *Nat. Mater.* 6(3), 183 (2007)
2. K. Wang, T. Hou, Y. Ren, and Z. Qiao, Enhanced robustness of zero-line modes in graphene via magnetic field, *Front. Phys.* 14(2), 23501 (2019)
3. J. Zeng, R. Xue, T. Hou, Y. Han, and Z. Qiao, Formation of topological domain walls and quantum transport properties of zero-line modes in commensurate bilayer graphene systems, *Front. Phys.* 17(6), 63503 (2022)
4. H. Yang, J. Zeng, S. You, Y. Han, and Z. Qiao, Equipartition of current in metallic armchair nanoribbon of graphene-based device, *Front. Phys.* 17(6), 63508 (2022)
5. Q. H. Wang, K. Kalantar-Zadeh, A. Kis, J. N. Coleman, and M. S. Strano, Electronics and optoelectronics of two-dimensional transition metal dichalcogenides, *Nat. Nanotechnol.* 7(11), 699 (2012)
6. G. Luo, Z. Z. Zhang, H. O. Li, X. X. Song, G. W. Deng, G. Cao, M. Xiao, and G. P. Guo, Quantum dot behavior in transition metal dichalcogenides nanostructures, *Front. Phys.* 12(4), 128502 (2017)
7. M. Cheng, J. Yang, X. Li, H. Li, R. Du, J. Shi, and J. He, Improving the device performances of two-dimensional semiconducting transition metal dichalcogenides: Three strategies, *Front. Phys.* 17(6), 63601 (2022)
8. D. J. Ibberson, L. Bourdet, J. C. Abadillo-Uriel, I. Ahmed, S. Barraud, M. J. Calderón, Y.M. Niquet, and M. F. Gonzalez-Zalba, Electric-field tuning of the valley splitting in silicon corner dots, *Appl. Phys. Lett.* 113(5), 053104 (2018)
9. M. Tahir, A. Manchon, K. Sabeeh, and U.

- Schwingenschlögl, Quantum spin/valley Hall effect and topological insulator phase transitions in silicene, *Appl. Phys. Lett.* 102(16), 162412 (2013)
10. C. J. Tabert and E. J. Nicol, AC/DC spin and valley Hall effects in silicene and germanene, *Phys. Rev. B* 87(23), 235426 (2013)
  11. Y. Li, J. Ludwig, T. Low, A. Chernikov, X. Cui, G. Arefe, Y. D. Kim, A. M. van der Zande, A. Rigosi, H. M. Hill, S. H. Kim, J. Hone, Z. Li, D. Smirnov, and T. F. Heinz, Valley splitting and polarization by the Zeeman effect in monolayer MoSe<sub>2</sub>, *Phys. Rev. Lett.* 113(26), 266804 (2014)
  12. C. Zhao, T. Norden, P. Zhang, P. Zhao, Y. Cheng, F. Sun, J. P. Parry, P. Taheri, J. Wang, Y. Yang, T. Scrase, K. Kang, S. Yang, G. X. Miao, R. Sabirianov, G. Kioseoglou, W. Huang, A. Petrou, and H. Zeng, Enhanced valley splitting in monolayer WSe<sub>2</sub> due to magnetic exchange field, *Nat. Nanotechnol.* 12(8), 757 (2017)
  13. S. Y. Li, Y. Su, Y. N. Ren, and L. He, Valley polarization and inversion in strained graphene via pseudo-Landau levels, valley splitting of real Landau levels, and confined states, *Phys. Rev. Lett.* 124(10), 106802 (2020)
  14. W. Yao, D. Xiao, and Q. Niu, Valley-dependent optoelectronics from inversion symmetry breaking, *Phys. Rev. B* 77(23), 235406 (2008)
  15. K. L. Seyler, D. Zhong, B. Huang, X. Linpeng, N. P. Wilson, T. Taniguchi, K. Watanabe, W. Yao, D. Xiao, M. A. McGuire, K. M. C. Fu, and X. Xu, Valley manipulation by optically tuning the magnetic proximity effect in WSe<sub>2</sub>/CrI<sub>3</sub> heterostructures, *Nano Lett.* 18(6), 3823 (2018)
  16. M. S. Mrudul, Á. Jiménez-Galán, M. Ivanov, and G. Dixit, Light-induced valleytronics in pristine graphene, *Optica* 8(3), 422 (2021)
  17. J. R. Schaibley, H. Yu, G. Clark, P. Rivera, J. S. Ross, K. L. Seyler, W. Yao, and X. Xu, Valleytronics in 2D materials, *Nat. Rev. Mater.* 1(11), 16055 (2016)
  18. D. Xiao, G. B. Liu, W. Feng, X. Xu, and W. Yao, Coupled spin and valley physics in monolayers of MoS<sub>2</sub> and other group-VI dichalcogenides, *Phys. Rev. Lett.* 108(19), 196802 (2012)
  19. K. Behnia, Polarized light boosts valleytronics, *Nat. Nanotechnol.* 7(8), 488 (2012)
  20. S. A. Wolf, D. D. Awschalom, R. A. Buhrman, J. M. Daughton, S. Von Molnár, M. L. Roukes, A. Y. Chtchelkanova, and D. M. Treger, Spintronics: A spin-based electronics vision for the future, *Science* 294(5546), 1488 (2001)
  21. A. Rycerz, J. Tworzydło, and C. Beenakker, Valley filter and valley valve in graphene, *Nat. Phys.* 3(3), 172 (2007)
  22. D. Pesin and A. H. MacDonald, Spintronics and pseudospintrronics in graphene and topological insulators, *Nat. Mater.* 11(5), 409 (2012)
  23. P. San-Jose, E. Prada, E. McCann, and H. Schomerus, Pseudospin valve in bilayer graphene: Towards graphene-based pseudospintrronics, *Phys. Rev. Lett.* 102(24), 247204 (2009)
  24. Y. S. Ang, S. A. Yang, C. Zhang, Z. Ma, and L. K. Ang, Valleytronics in merging Dirac cones: All-electric-controlled valley filter, valve, and universal reversible logic gate, *Phys. Rev. B* 96(24), 245410 (2017)
  25. J. Li, R.X. Zhang, Z. Yin, J. Zhang, K. Watanabe, T. Taniguchi, C. Liu, and J. Zhu, A valley valve and electron beam splitter, *Science* 362(6419), 1149 (2018)
  26. F. D. M. Haldane, Model for a quantum Hall effect without Landau levels: Condensed-matter realization of the “parity anomaly”, *Phys. Rev. Lett.* 61(18), 2015 (1988)
  27. Y. Ren, Z. Qiao, and Q. Niu, Topological phases in two-dimensional materials: A review, *Rep. Prog. Phys.* 79(6), 066501 (2016)
  28. C. Z. Chang, J. Zhang, X. Feng, J. Shen, Z. Zhang, M. Guo, K. Li, Y. Ou, P. Wei, L. Wang, Z. Ji, Y. Feng, S. Ji, X. Chen, J. Jia, X. Dai, Z. Fang, S. C. Zhang, K. He, Y. Wang, L. Lu, X. C. Ma, and Q. K. Xue, Experimental observation of the quantum anomalous Hall effect in a magnetic topological insulator, *Science* 340(6129), 167 (2013)
  29. Y. Deng, Y. Yu, M. Z. Shi, Z. Guo, Z. Xu, J. Wang, X. H. Chen, and Y. Zhang, Quantum anomalous Hall effect in intrinsic magnetic topological insulator MnBi<sub>2</sub>Te<sub>4</sub>, *Science* 367(6480), 895 (2020)
  30. Z. Qiao, S. A. Yang, W. Feng, W. K. Tse, J. Ding, Y. Yao, J. Wang, and Q. Niu, Quantum anomalous Hall effect in graphene from Rashba and exchange effects, *Phys. Rev. B* 82(16), 161414 (2010)
  31. Z. Qiao, W. Ren, H. Chen, L. Bellaiche, Z. Zhang, A. H. MacDonald, and Q. Niu, Quantum anomalous Hall effect in graphene proximity coupled to an antiferromagnetic insulator, *Phys. Rev. Lett.* 112(11), 116404 (2014)
  32. R. Yu, W. Zhang, H. J. Zhang, S. C. Zhang, X. Dai, and Z. Fang, Quantized anomalous Hall effect in magnetic topological insulators, *Science* 329(5987), 61 (2010)
  33. J. Zhang, B. Zhao, T. Zhou, Y. Xue, C. Ma, and Z. Yang, Strong magnetization and Chern insulators in compressed graphene/CrI<sub>3</sub> van der Waals heterostructures, *Phys. Rev. B* 97(8), 085401 (2018)
  34. J. Kim, X. Hong, C. Jin, S. F. Shi, C. Y. S. Chang, M. H. Chiu, L. J. Li, and F. Wang, Ultrafast generation of pseudo-magnetic field for valley excitons in WSe<sub>2</sub> monolayers, *Science* 346(6214), 1205 (2014)
  35. A. Srivastava, M. Sidler, A. V. Allain, D. S. Lembke, A. Kis, and A. Imamoglu, Valley Zeeman effect in elementary optical excitations of monolayer WSe<sub>2</sub>, *Nat. Phys.* 11(2), 141 (2015)
  36. H. Rostami and R. Asgari, Valley Zeeman effect and spin-valley polarized conductance in monolayer MoS<sub>2</sub> in a perpendicular magnetic field, *Phys. Rev. B* 91(7), 075433 (2015)
  37. Y. Li, J. Ludwig, T. Low, A. Chernikov, X. Cui, G. Arefe, Y. D. Kim, A. M. van der Zande, A. Rigosi, H. M. Hill, S. H. Kim, J. Hone, Z. Li, D. Smirnov, and T. F. Heinz, Valley splitting and polarization by the Zeeman effect in monolayer MoSe<sub>2</sub>, *Phys. Rev. Lett.* 113(26), 266804 (2014)
  38. Z. Liu, Y. Han, Y. Ren, Q. Niu, and Z. Qiao, .Van der

- Waals heterostructure  $\text{Pt}_2\text{HgSe}_3/\text{CrI}_3$  for topological valleytronics, *Phys. Rev. B* 104(12), L121403 (2021)
39. M. Bora, S. K. Behera, P. Samal, and P. Deb, Magnetic proximity induced valley-contrasting quantum anomalous Hall effect in a graphene-CrBr<sub>3</sub> van der Waals heterostructure, *Phys. Rev. B* 105(23), 235422 (2022)
40. H. Zhang, W. Yang, Y. Ning, and X. Xu, Abundant valley-polarized states in two-dimensional ferromagnetic van der Waals heterostructures, *Phys. Rev. B* 101(20), 205404 (2020)
41. M. Vila, J. H. Garcia, and S. Roche, Valley-polarized quantum anomalous Hall phase in bilayer graphene with layer-dependent proximity effects, *Phys. Rev. B* 104(16), L161113 (2021)
42. M. U. Rehman, Z. Qiao, and J. Wang, Valley-symmetry-broken magnetic topological responses in  $(\text{Pt}/\text{Pd})_2\text{HgSe}_3/\text{CrGeTe}_3$  and  $\text{Pd}_2\text{HgSe}_3/\text{CrI}_3$  through interfacial coupling, *Phys. Rev. B* 105(16), 165417 (2022)
43. M. U. Rehman, M. Kiani, and J. Wang, Jacutingaite family: An efficient platform for coexistence of spin valley Hall effects. valley spin-valve realization and layer spin crossover, *Phys. Rev. B* 105(19), 195439 (2022)
44. H. Pan, Z. Li, C. C. Liu, G. Zhu, Z. Qiao, and Y. Yao, Valley-polarized quantum anomalous Hall effect in silicene, *Phys. Rev. Lett.* 112(10), 106802 (2014)
45. J. Zhou, Q. Sun, and P. Jena, Valley-polarized quantum anomalous Hall effect in ferrimagnetic honeycomb lattices, *Phys. Rev. Lett.* 119(4), 046403 (2017)
46. Z. Liu, Y. Ren, Y. Han, Q. Niu, and Z. Qiao, Second-order topological insulator in van der Waals heterostructures of  $\text{CoBr}_2/\text{Pt}_2\text{HgSe}_3/\text{CoBr}_2$ , arXiv: 2202.00221 (2022)
47. F. Zhan, Z. Ning, L.Y. Gan, B. Zheng, J. Fan, and R. Wang, Floquet valley-polarized quantum anomalous Hall state in nonmagnetic heterobilayers, *Phys. Rev. B* 105(8), L081115 (2022)
48. I. Cucchi, A. Marrazzo, E. Cappelli, S. Ricco, F. Y. Bruno, S. Lisi, M. Hoesch, T. K. Kim, C. Cacho, C. Besnard, E. Giannini, N. Marzari, M. Gibertini, F. Baumberger, and A. Tamai, Bulk and surface electronic structure of the dual-topology semimetal  $\text{Pt}_2\text{HgSe}_3$ , *Phys. Rev. Lett.* 124(10), 106402 (2020)
49. K. Kandrai, P. Vancsó, G. Kukucska, J. Koltai, G. Baranka, Á. Hoffmann, Á. Pekker, K. Kamarás, Z. E. Horváth, A. Vymazalová, L. Tapasztó, and P. Nemes-Incze, Signature of large-gap quantum spin Hall state in the layered mineral jacutingaite, *Nano Lett.* 20(7), 5207 (2020)
50. A. Marrazzo, M. Gibertini, D. Campi, N. Mounet, and N. Marzari, Prediction of a large-gap and switchable Kane-Mele quantum spin Hall insulator, *Phys. Rev. Lett.* 120(11), 117701 (2018)
51. A. Marrazzo, M. Gibertini, D. Campi, N. Mounet, and N. Marzari, Relative abundance of  $Z_2$  topological order in exfoliable two-dimensional insulators, *Nano Lett.* 19(12), 8431 (2019)
52. C. L. Kane and E. J. Mele,  $Z_2$  topological order and the quantum spin Hall effect, *Phys. Rev. Lett.* 95(14), 146802 (2005)
53. F. C. de Lima, R. H. Miwa, and A. Fazzio, Jacutingaite-family: A class of topological materials, *Phys. Rev. B* 102(23), 235153 (2020)
54. C. Ma, H. Forster, and G. Grundmann, Tilkerodeite,  $\text{Pd}_2\text{HgSe}_3$ , a new platinum-group mineral from Tilkerode, Harz Mountains, Germany, *Crystals (Basel)* 10(8), 687 (2020)
55. A. Marrazzo, N. Marzari, and M. Gibertini, Emergent dual topology in the three-dimensional Kane-Mele  $\text{Pt}_2\text{HgSe}_3$ , *Phys. Rev. Res.* 2(1), 012063 (2020)
56. M. A. McGuire, Crystal and magnetic structures in layered, transition metal dihalides and trihalides, *Crystals (Basel)* 7(5), 121 (2017)
57. V. V. Kulish and W. Huang, Single-layer metal halides  $\text{MX}_2$  ( $X = \text{Cl}, \text{Br}, \text{I}$ ): Stability and tunable magnetism from first principles and Monte Carlo simulations, *J. Mater. Chem. C* 5(34), 8734 (2017)
58. B. Huang, G. Clark, E. Navarro-Moratalla, D. R. Klein, R. Cheng, K. L. Seyler, D. Zhong, E. Schmidgall, M. A. McGuire, D. H. Cobden, W. Yao, D. Xiao, P. Jarillo-Herrero, and X. Xu, Layer-dependent ferromagnetism in a van der Waals crystal down to the monolayer limit, *Nature* 546(7657), 270 (2017)
59. M. M. Otkrov, I. P. Rusinov, M. Blanco-Rey, M. Hoffmann, A. Yu. Vyazovskaya, S. V. Eremeev, A. Ernst, P. M. Echenique, A. Arnau, and E. V. Chulkov, Unique thickness-dependent properties of the van der waals interlayer antiferromagnet  $\text{MnBi}_2\text{Te}_4$  films, *Phys. Rev. Lett.* 122(10), 107202 (2019)
60. S. Tian, J. F. Zhang, C. Li, T. Ying, S. Li, X. Zhang, K. Liu, and H. Lei, Ferromagnetic van der Waals crystal  $\text{VI}_3$ , *J. Am. Chem. Soc.* 141(13), 5326 (2019)
61. H. Y. Lv, W. J. Lu, X. Luo, X. B. Zhu, and Y. P. Sun, Strain- and carrier-tunable magnetic properties of a two-dimensional intrinsically ferromagnetic semiconductor:  $\text{CoBr}_2$  monolayer, *Phys. Rev. B* 99(13), 134416 (2019)
62. A. S. Botana and M. R. Norman, Electronic structure and magnetism of transition metal dihalides: Bulk to monolayer, *Phys. Rev. Mater.* 3(4), 044001 (2019)
63. M. M. Otkrov, I. P. Rusinov, M. Blanco-Rey, M. Hoffmann, A. Yu. Vyazovskaya, S. V. Eremeev, A. Ernst, P. M. Echenique, A. Arnau, and E. V. Chulkov, Unique thickness-dependent properties of the van der Waals interlayer antiferromagnet  $\text{MnBi}_2\text{Te}_4$  films, *Phys. Rev. Lett.* 122(10), 107202 (2019)
64. X. Li, Z. Zhang, and H. Zhang, High throughput study on magnetic ground states with Hubbard  $U$  corrections in transition metal dihalide monolayers, *Nanoscale Adv.* 2(1), 495 (2020)
65. M. Lu, Q. Yao, C. Xiao, C. Huang, and E. Kan, Mechanical, electronic, and magnetic properties of  $\text{NiX}_2$  ( $X = \text{Cl}, \text{Br}, \text{I}$ ) layers, *ACS Omega* 4(3), 5714 (2019)
66. D. Zhong, K. L. Seyler, X. Linpeng, R. Cheng, N. Sivadas, B. Huang, E. Schmidgall, T. Taniguchi, K. Watanabe, M. A. McGuire, W. Yao, D. Xiao, K. M. C. Fu, and X. Xu, Van der Waals engineering of ferromagnetic semiconductor heterostructures for spin and valleytronics, *Sci. Adv.* 3(5), e1603113 (2017)
67. L. Webster and J. A. Yan, Strain-tunable magnetic anisotropy in monolayer  $\text{CrCl}_3$ ,  $\text{CrBr}_3$ , and  $\text{CrI}_3$ , *Phys.*

- Rev. B* 98(14), 144411 (2018)
68. C. Gong, L. Li, Z. Li, H. Ji, A. Stern, Y. Xia, T. Cao, W. Bao, C. Wang, Y. Wang, Z. Q. Qiu, R. J. Cava, S. G. Louie, J. Xia, and X. Zhang, Discovery of intrinsic ferromagnetism in two-dimensional van der Waals crystals, *Nature* 546(7657), 265 (2017)
  69. S. Jiang, J. Shan, and K. F. Mak, Electric-field switching of two-dimensional van der Waals magnets, *Nat. Mater.* 17(5), 406 (2018)
  70. K. F. Mak, J. Shan, and D. C. Ralph, Probing and controlling magnetic states in 2D layered magnetic materials, *Nat. Rev. Phys.* 1(11), 646 (2019)
  71. W. Zhuo, B. Lei, S. Wu, F. Yu, C. Zhu, J. Cui, Z. Sun, D. Ma, M. Shi, H. Wang, W. Wang, T. Wu, J. Ying, S. Wu, Z. Wang, and X. Chen, Manipulating ferromagnetism in few-layered Cr<sub>2</sub>Ge<sub>2</sub>Te<sub>6</sub>, *Adv. Mater.* 33(31), 2008586 (2021)
  72. See Supplemental Materials for more information about calculation details, ferromagnetic substrates, vdW heterostructue configurations, orbital projections, molecular dynamic simulations, more band structures, manipulated band gaps, charge density differences and the planar-averaged electrostatic potentials of other well-matched systems.
  73. P. E. Blöchl, Projector augmented-wave method, *Phys. Rev. B* 50(24), 17953 (1994)
  74. G. Kresse and J. Furthmüller, Efficient iterative schemes for ab initio total-energy calculations using a plane-wave basis set, *Phys. Rev. B* 54(16), 11169 (1996)
  75. G. Kresse and D. Joubert, From ultrasoft pseudopotentials to the projector augmented-wave method, *Phys. Rev. B* 59(3), 1758 (1999)
  76. J. P. Perdew, J. A. Chevary, S. H. Vosko, K. A. Jackson, M. R. Pederson, D. J. Singh, and C. Fiolhais, Atoms, molecules, solids, and surfaces: Applications of the generalized gradient approximation for exchange and correlation, *Phys. Rev. B* 46(11), 6671 (1992)
  77. S. Grimme, J. Antony, S. Ehrlich, and H. Krieg, A consistent and accurate ab initio parametrization of density functional dispersion correction (DFT-D) for the 94 elements H-Pu, *J. Chem. Phys.* 132(15), 154104 (2010)
  78. H. J. Kulik, M. Cococcioni, D. A. Scherlis, and N. Marzari, Density functional theory in transition-metal chemistry: A self-consistent Hubbard *U* approach, *Phys. Rev. Lett.* 97(10), 103001 (2006)
  79. A. A. Mostofi, J. R. Yates, Y. S. Lee, I. Souza, D. Vanderbilt, and N. Marzari, Wannier90: A tool for obtaining maximally-localised Wannier functions, *Comput. Phys. Commun.* 178(9), 685 (2008)
  80. G. Pizzi, V. Vitale, R. Arita, S. Blugel, F. Freimuth, G. Geranton, M. Gibertini, D. Gresch, C. Johnson, T. Koretsune, J. Ibañez-Azpiroz, H. Lee, J.M. Lihm, D. Marchand, A. Marrazzo, Y. Mokrousov, J. I. Mustafa, Y. Nohara, Y. Nomura, L. Paulatto, S. Poncé, T. Ponweiser, J. Qiao, F. Thöle, S. S. Tsirkin, M. Wierzbowska, N. Marzari, D. Vanderbilt, I. Souza, A. A. Mostofi, and J. R. Yates, Wannier90 as a community code: new features and applications, *J. Phys.: Condens. Matter* 32(16), 165902 (2020)
  81. Q. S. Wu, S. N. Zhang, H. F. Song, M. Troyer, and A. A. Soluyanov, WannierTools: An open-source software package for novel topological materials, *Comput. Phys. Commun.* 224, 405 (2018)
  82. V. Wang, N. Xu, J. C. Liu, G. Tang, and W. T. Geng, VASPKIT: A user-friendly interface facilitating high-throughput computing and analysis using VASP code, *Comput. Phys. Commun.* 267, 108033 (2021)
  83. U. Herath, P. Tavadze, X. He, E. Bousquet, S. Singh, F. Munoz, and A. H. Romero, PyProcar: A Python library for electronic structure pre/post-processing, *Comput. Phys. Commun.* 251 80(2020) (1070)
  84. K. Momma and F. Izumi, VESTA3 for three-dimensional visualization of crystal, volumetric and morphology data, *J. Appl. Cryst.* 44(6), 1272 (2011)
  85. M. H. Chiu, C. Zhang, H. W. Shiu, C. P. Chuu, C. H. Chen, C. Y. S. Chang, C. H. Chen, M. Y. Chou, C. K. Shih, and L. J. Li, Determination of band alignment in the single-layer MoS<sub>2</sub>/WSe<sub>2</sub> heterojunction, *Nat. Commun.* 6(1), 7666 (2015)
  86. V. O. Özçelik, J. G. Azadani, C. Yang, S. J. Koester, and T. Low, Band alignment of two-dimensional semiconductors for designing heterostructures with momentum space matching, *Phys. Rev. B* 94(3), 035125 (2016)
  87. C. Xia, J. Du, M. Li, X. Li, X. Zhao, T. Wang, and J. Li, Effects of electric field on the electronic structures of broken-gap phosphorene/SnX<sub>2</sub> (X = S, Se) van der Waals heterojunctions, *Phys. Rev. Appl.* 10(5), 054064 (2018)
  88. C. Lei, Y. Ma, X. Xu, T. Zhang, B. Huang, and Y. Dai, Broken-gap type-III band alignment in WTe<sub>2</sub>/HfS<sub>2</sub> van der Waals heterostructure, *J. Phys. Chem. C* 123(37), 23089 (2019)
  89. X. R. Hu, J. M. Zheng, and Z. Y. Ren, Strong interlayer coupling in phosphorene/graphene van der Waals heterostructure: A first-principles investigation, *Front. Phys.* 13(2), 137302 (2018)
  90. Z. Z. Yan, Z. H. Jiang, J. P. Lu, and Z. H. Ni, Interfacial charge transfer in WS<sub>2</sub> monolayer/CsPbBr<sub>3</sub> microplate heterostructure, *Front. Phys.* 13(4), 138115 (2018)
  91. Y. Y. Wang, F. P. Li, W. Wei, B. B. Huang, and Y. Dai, Interlayer coupling effect in van der Waals heterostructures of transition metal dichalcogenides, *Front. Phys.* 16(1), 13501 (2021)
  92. C. Zhao, T. Norden, P. Zhang, P. Zhao, Y. Cheng, F. Sun, J. P. Parry, P. Taheri, J. Wang, Y. Yang, T. Scrase, K. Kang, S. Yang, G. Miao, R. Sabirianov, G. Kioseoglou, W. Huang, A. Petrou, and H. Zeng, Enhanced valley splitting in monolayer WSe<sub>2</sub> due to magnetic exchange field, *Nat. Nanotechnol.* 12(8), 757 (2017)
  93. T. Norden, C. Zhao, P. Zhang, R. Sabirianov, A. Petrou, and H. Zeng, Giant valley splitting in monolayer WS<sub>2</sub> by magnetic proximity effect, *Nat. Commun.* 10(1), 4163 (2019)
  94. X. Deng, H. Yang, S. Qi, X. Xu, and Z. Qiao, Quantum anomalous Hall effect and giant Rashba spin-orbit splitting in graphene system co-doped with boron and 5d transition-metal atoms, *Front. Phys.* 13(5), 137308 (2018)

95. Y. Han, S. Sun, S. Qi, X. Xu, and Z. Qiao, Interlayer ferromagnetism and high-temperature quantum anomalous Hall effect in p-doped  $\text{MnBi}_2\text{Te}_4$  multilayers, *Phys. Rev. B* 103(24), 245403 (2021)
96. S. Qi, R. Gao, M. Chang, Y. Han, and Z. Qiao, Pursuing the high-temperature quantum anomalous Hall effect in  $\text{MnBi}_2\text{Te}_4/\text{Sb}_2\text{Te}_3$  heterostructures, *Phys. Rev. B* 101(1), 014423 (2020)
97. S. Qi, Z. Qiao, X. Deng, E. D. Cubuk, H. Chen, W. Zhu, E. Kaxiras, S. B. Zhang, X. Xu, and Z. Zhang, High-temperature quantum anomalous Hall effect in n-p codoped topological insulators, *Phys. Rev. Lett.* 117(5), 056804 (2016)
98. Z. Li, Y. Han, and Z. Qiao, Chern number tunable quantum anomalous Hall effect in monolayer transitional metal oxides via manipulating magnetization orientation, *Phys. Rev. Lett.* 129(3), 036801 (2022)
99. Y. Han, Z. Yan, Z. Li, X. Xu, Z. Zhang, Q. Niu, and Z. Qiao, Large Rashba spin-orbit coupling and high-temperature quantum anomalous Hall effect in Re-intercalated graphene/ $\text{CrI}_3$  heterostructure, arXiv: 2203.16429 (2022)